

Chemical vapor deposition synthesis of $(\text{GeTe})_n(\text{Sb}_2\text{Te}_3)$ gradient crystalline films as promising planar heterostructures

M. Zhezhu^{1,*}, A. Vasil'ev¹, M. Yapryntsev², E. Ghalumyan³, D. A. Ghazaryan^{4,5}, H. Gharagulyan^{1,3,*}

¹*A.B. Nalbandyan Institute of Chemical Physics NAS RA, Yerevan 0014, Armenia*

²*Belgorod State University, Belgorod 308000, Russia*

³*Institute of Physics, Yerevan State University, Yerevan 0025, Armenia*

⁴*Moscow Center for Advanced Studies, Kulakova str. 20, Moscow 123592, Russia*

⁵*Laboratory of Advanced Functional Materials, Yerevan State University, Yerevan 0025, Armenia*

**The correspondence should be addressed to:*

marina.zhezhu@ichph.sci.am and herminegharagulyan@ysu.am

Abstract

Phase-change materials of the $(\text{GeTe})_n(\text{Sb}_2\text{Te}_3)$ (GST) system are of high relevance in memory storage and energy conversion applications due to their fast-switching speed, high data retention, and tunable properties. Here, we report on a fast and efficient CVD-based method for the fabrication of crystalline GST films with variable Ge/Sb atomic content. In particular, the approach enables compositional control without changing the precursor, facilitating a gradient synthesis of $\text{Ge}_3\text{Sb}_2\text{Te}_6$, $\text{Ge}_2\text{Sb}_2\text{Te}_5$, and GeSb_2Te_4 phases in a single attempt. The analyses of their structural, optical, and electrical aspects highlight how compositional variation influences the film's properties. Our findings demonstrate a straightforward approach enabling the preparation of gradient crystalline GST films with tunable morphology and functionality. These gradient films can potentially provide in-plane multilevel and gradual switching thresholds for memory applications and altered refractive index and absorption for optical modulation and filtering applications.

Keywords: phase-change materials, chemical vapor deposition, $(\text{GeTe})_n(\text{Sb}_2\text{Te}_3)$, gradient crystalline films.

Abbreviations: GST: $(\text{GeTe})_n(\text{Sb}_2\text{Te}_3)$; CVD: chemical vapor deposition.

1. Introduction

Phase-change materials based on the GeTe – Sb_2Te_3 pseudobinary system are best known for their use in optical data storage and nonvolatile memory devices [1, 2]. In recent years, their unique physical properties have also sparked a growing interest in emerging applications, such as thermoelectrics, sensors, neuromorphic computing, and infrared photonics [3-6]. $(\text{GeTe})_n(\text{Sb}_2\text{Te}_3)$ (GST) films are typically deposited using physical vapor deposition (PVD) methods, such as magnetron sputtering and pulsed laser deposition that produces amorphous films [7, 8]. Chemical vapor deposition (CVD) is a promising alternative to PVD methods for fabricating high-quality GST films [9, 10]. While PVD methods are widely used to produce homogeneous amorphous films, they often require high-vacuum systems and costly equipment. In addition, sputtered films are more prone to contamination from the sputtering gas and typically exhibit higher defect densities due to the high-energy impact of arriving atoms [11]. In contrast, CVD enables material transport and deposition at lower kinetic energies and under moderate vacuum conditions, thereby reducing equipment complexity and impurity incorporation. CVD also offers superior composition control, allowing for uniform and conformal film growth even on complex surfaces [12]. Although CVD processes may involve higher energy consumption, they provide better crystallinity and lower defect densities, which is particularly advantageous for the fabrication of multi-component and layered heterostructured films [13]. However, using metal-organic precursors in CVD processes raises significant safety concerns due to their toxicity

and pyrophoric nature. Crystallization of the obtained amorphous films into either the metastable cubic phase or the thermodynamically stable hexagonal phase can subsequently be induced via Joule heating or by applying electrical, optical, or laser pulses [14, 15]. Additionally, superlattice-structured GST materials, such as $(\text{GeTe})_n/(\text{Sb}_2\text{Te}_3)$, have recently attracted attention for advanced phase-change and thermoelectric applications due to their tailored electronic band structures, suppressed thermal conductivity, and enhanced switching performance [16-19]. Hexagonal phases of GST alloys demonstrate significant potential for thermoelectric applications owing to their combination of high electrical conductivity and low thermal conductivity [3]. Moreover, their favorable electronic structure and exceptional optical properties make them attractive for optoelectronic applications [20-22]. Among GST alloys, $\text{Ge}_3\text{Sb}_2\text{Te}_6$, $\text{Ge}_2\text{Sb}_2\text{Te}_5$, and GeSb_2Te_4 —the most extensively studied composition—are located along the pseudobinary tie line between GeTe and Sb_2Te_3 . All hexagonal GST compounds are narrow bandgap semiconductors that exhibit intrinsic *p*-type conduction. They are characterized by high electrical conductivity ($\sim 10^5$ S/m) at room temperature [3]. Regarding optical properties, $\text{Ge}_2\text{Sb}_2\text{Te}_5$ is a promising broadband infrared absorber, attracting significant attention for optoelectronic applications [6]. Several studies highlighted the potential of this material as an efficient broadband absorber in the infrared region [22, 23]. Multilayer structures incorporating crystalline $\text{Ge}_2\text{Sb}_2\text{Te}_5$ demonstrated absorption levels as high as 93.6 % in the 1–1.6 μm wavelength range [6]. Furthermore, the inclusion of $\text{Ge}_2\text{Sb}_2\text{Te}_5$ significantly enhances the performance of plasmonic metasurface absorbers, achieving a maximum absorption of 99.56% in the 740–920 nm range for the hexagonal crystalline phase of the GST-coated layer [24]. Variation in their Ge/Sb/Te atomic ratios results in various structural characteristics and physical properties, providing a versatile platform for exploring structure-property relationships for future applications [3-6, 22-24]. While using crystalline gradient GST materials in photonics has not yet been widely explored, they hold significant potential for future applications. Particularly, a lateral compositional gradient in GST-based heterostructures offers a promising option for advanced photonic applications. It enables spatial tuning of optical properties, such as refractive index and absorption across the film, allowing for precise control of light propagation and interaction within a single device. This functionality can be exploited for optical modulation, where different regions of the film respond variably to external stimuli, like temperature and light, enabling dynamic modulation of transmission or reflection profiles. In spatial light control, the gradient can serve as a passive platform for beam shaping, focusing, and steering, with potential use in flat optics and metasurfaces [25-27]. Overall, the gradient GST design adds functional versatility and makes it suitable for compact, tunable, and highly integrated photonic devices.

This study aims to develop a simple method for the simultaneous CVD synthesis of GST films with tunable Ge/Sb compositions and to compare their structural, electrical, and optical properties for potential applications in electronic and optoelectronic devices. Designing gradient films of these materials with controlled electrooptical properties through compositional tuning allows them to be used in a single device. Specifically, we focus on the detailed analysis of the film's composition, microstructure, and morphology, aiming to reveal differences in elemental distribution across the deposited films and changes in morphology and grain size as a function of distance from the source. The gradient absorption properties, influenced by the film composition and crystallite size, open up opportunities for applying these films in near-infrared (NIR) optical sensors, where controlled signal attenuation is required, as well as in infrared (IR) shielding components and heat-absorbing photonic windows with spatially selective absorbance.

2. Experimental method

A $\text{Ge}_2\text{Sb}_2\text{Te}_5$ source crystal was grown beforehand to prepare the GST films. High-purity elemental precursors Ge (99.999%), Sb (99.999%), and Te (99.99%) were weighed in stoichiometric proportions

corresponding to the nominal composition of $\text{Ge}_2\text{Sb}_2\text{Te}_5$. The reagents were sealed in an evacuated quartz ampoule, which was then gradually heated to 1000°C and held at this temperature for 2 h to ensure homogenization of the mixture and reaction between the elements. Subsequently, the ampoule was slowly cooled to allow the crystallization of the desired alloy. The resulting bulk alloy was cleaved using Scotch tape and characterized using X-ray diffraction (XRD), Raman spectroscopy, and scanning electron microscopy (SEM) methods.

Furthermore, this crystal, serving as a source material, was placed at the center of the heating zone inside a quartz tube with a diameter of 50 mm. Then, the polycrystalline Al_2O_3 substrates (1×1 cm) were positioned at varying distances (10–14 cm) from the source. During the deposition process, a constant vacuum of 10 Pa was maintained. The reaction tube was heated to 550°C over 30 minutes and held at this temperature for 30 minutes. The tube was rapidly removed from the heating zone to terminate the deposition. The GST films are labeled as follows: Film 1 corresponds to a source-to-substrate distance of 14 cm; Film 2 to 13 cm; Film 3 to 12 cm; Film 4 to 11 cm; and Film 5 to 10 cm. The obtained nanostructured films were characterized and analyzed using XRD analysis with grazing incidence (GIXRD, Rigaku Ultima IV diffractometer with CuK_α -radiation), SEM (Nova NanoSEM 450 microscope), atomic force microscopy and Raman spectroscopy (AFM-combined Raman spectrometer by LabRAM HR Evolution, HORIBA), optical spectroscopy (NIR Spectrometer 900–2500 nm, StellarNet, Inc.), and four-point probe electrical analysis (Veeco Instruments, Inc.).

3. Result and discussion

Fig. S1(a-c) presents the characterization of the synthesized source material. EDS analysis of the crystal fracture surface revealed the presence of 20.4 at.% Ge, 25.3 at.% Sb, and 54.3 at.% Te. The XRD diffractogram corresponds to the $\text{P}\bar{3}\text{m1}$ space group and confirms the formation of a single-phase $\text{Ge}_2\text{Sb}_2\text{Te}_5$ crystal. The Raman spectrum of the obtained crystal contains both sharp and broad spectral features. The sharp lines are attributed to phonon modes originating from Sb_2Te_3 , which serves as the structural basis of GST, while the broad bands might be associated with Ge/Sb disorder [28]. $\text{Ge}_2\text{Sb}_2\text{Te}_5$, considered a quasibinary alloy of $(\text{GeTe})_n(\text{Sb}_2\text{Te}_3)$ with $n = 2$, represents an intermediate composition along the Sb_2Te_3 -GeTe tie line. When used as a source material in the CVD process, it is expected to enable compositional gradient deposition of GST films due to preferential vapor transport and phase separation tendencies. As schematically illustrated in Fig. 1(a), the $\text{Ge}_2\text{Sb}_2\text{Te}_5$ crystal was placed in the hot zone, whereas the substrates were positioned in the cold zone at a distance of 10–14 cm. The $\text{Ge}_2\text{Sb}_2\text{Te}_5$ precursor was heated to 550°C since heating to 640°C and above can lead to the deposition of elemental (0-valent) Ge [29]. Initially, the composition, microstructure, and morphology of the films deposited on the substrates were analyzed (Fig. 1(b–f) and Fig. S2 (a–e)). EDS analysis demonstrates the differences in elemental distribution across the deposited films (Table 1). Here, Film 3, positioned at an intermediate distance, exhibits a Ge/Sb = 1.

In contrast, Films 1 and 2 exhibit a higher Ge content relative to Sb, while Films 4 and 5 are enriched in Sb compared to Ge. Similar to the variation in elemental composition, morphology and grain size exhibit distinct changes as a function of distance from the source. Films 1–4 (see Fig. 1(b–e) and Fig. S2(a–d)) are mainly composed of plates growing perpendicular to the substrate, occasionally forming flower-like clusters and exhibiting plates with angular shapes. The plate size is characterized by the length (l) (Table 1), thickness (d), and l/d ratio (Table S2). The plate length gradually decreases with increasing source-to-substrate distance from $3.31 \mu\text{m}$ for Film 4 to $0.37 \mu\text{m}$ for Film 1. On the contrary, Film 5 displays signs of plate merging, with stacked partially fused or overlapped structures, indicating recrystallization after deposition. Fig. S2(a) clearly illustrates the small plates that form Film 1, while Fig. S2(e) reveals the overlapped, recrystallized plates.

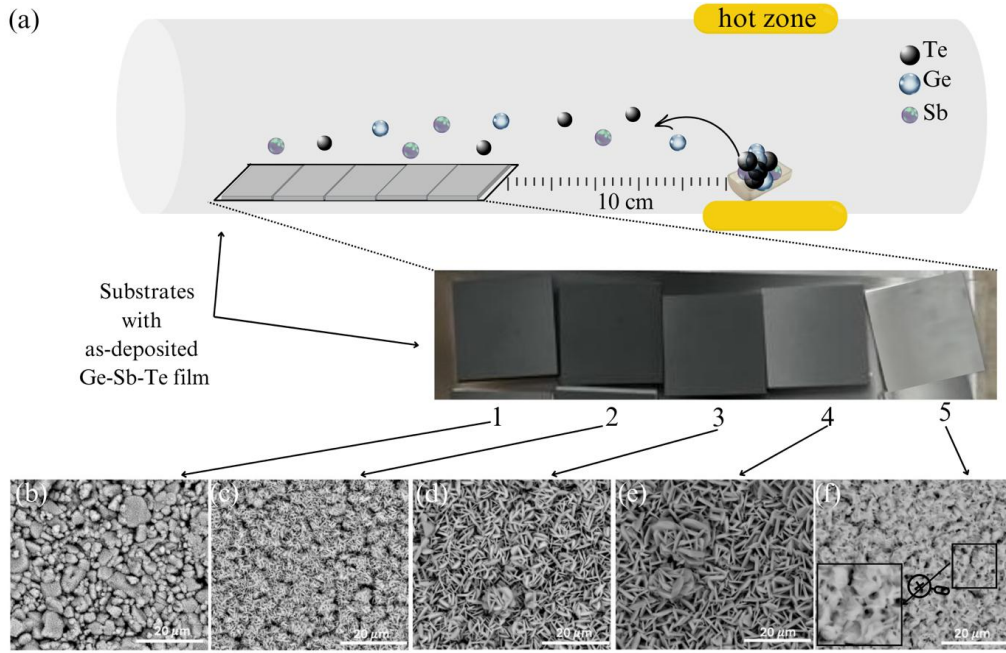


Fig. 1. Schematic illustration of the chemical vapor deposition process of GST films (a) along with the corresponding SEM images of the film's surface deposited on each substrate: Film 1 (b), Film 2 (c), Film 3 (d), Film 4 (e), and Film 5 (f), respectively. The zoomed-in area of Film 5 illustrates its recrystallization.

Additionally, R_{ms} values were determined from AFM scans performed over an area of $10 \times 10 \mu\text{m}^2$ (Table 1). According to the obtained data, the films exhibit relatively high roughness, with the minimal R_{ms} being $0.37 \mu\text{m}$ for Film 1. Thus, Film 1, positioned 14 cm from the source, shows the smallest plate size and lowest R_{ms} . Details of the morphological analysis are provided in the SI, and additional information on plate sizes is listed in Table S1.

Compared to crystalline GST films fabricated by magnetron sputtering [30], which typically exhibit a more homogeneous morphology and lower surface roughness after annealing of the as-deposited amorphous films, the CVD-grown films in our study demonstrate a distinctly different structure. These films consist of plate-like crystallites arranged into flower-like assemblies, resulting in a more textured surface with increased roughness. This morphological contrast arises from CVD enabling direct crystallization during deposition under varying temperature conditions, resulting in a more structurally diverse surface morphology [11].

A temperature gradient was established due to the source being located in the hot zone and the substrates positioned in the cold zone, with the gradient depending on the distance between them. To reliably assess the temperature distribution across the cold zone, a control (blank) experiment was conducted under the same thermal conditions as those used in the chemical deposition process. As a result, the deposition temperatures were determined to be approximately 195°C for Film 1, 227°C for Film 2, 286°C for Film 3, 378°C for Film 4, and 444°C for Film 5, depending on the distance from the hot zone. The measurement scheme is shown in Fig. S3(a), and the obtained data are graphically presented in Fig. S3(b).

The deposition temperature is one of the most important parameters influencing the final grain structure of a vapor-deposited film for a given material system [11]. Specifically, according to classical nucleation theory, at low temperatures or in the presence of high diffusion barriers, adatoms - individual atoms that land on a surface during film deposition and can move or diffuse before becoming part of the solid film structure- tend to remain at their landing sites, resulting in amorphous or fine-grained polycrystalline film structures. As the temperature increases, enhanced surface diffusion allows

adatoms to travel longer distances and coalesce into stable clusters, promoting the formation of larger grains [11]. Consistent with this, at elevated deposition temperatures, enhanced atomic diffusion decreases nucleation density, promoting the growth of larger grains and more continuous films. Conversely, lower temperatures limit atomic mobility, leading to higher nucleation density, smaller grain sizes, and a rougher surface morphology [31]. A correlation between increased deposition temperature, enlarged grain size, and surface morphology was also observed in GST films fabricated via the CVD method [32]. The thicknesses of the films were estimated from cross-sectional SEM images, and the obtained values range from 1.05 to 2.97 μm (Table 1).

The scaling of this deposition process would require the implementation of temperature-controlled zones of appropriate dimensions to ensure full coverage of the target area, the use of a larger-diameter quartz tube, and the ability to rapidly terminate the deposition process by shifting the quartz tube into a cold zone to stop material deposition immediately.

Table 1. Structural and morphological characteristics of the GST films.

Sample	EDS analysis			Morphologic al analysis		t μm	XRD analysis			Film identificat ion
	Ge, at. %	Sb, at. %	Te, at. %	l , μm	R_{ms} , μm		Lattice parameters		Space group	
							a, b (Å)	c (Å)		
Film 1	28.0	16.6	55.4	0.37	0.37	1.16	4.2601	61.10	$R\bar{3}m$	$\text{Ge}_3\text{Sb}_2\text{Te}_6$
Film 2	26.4	18.0	55.7	1.16	0.75	2.97	4.2104	61.718		
Film 3	22.4	21.9	55.7	2.11	0.57	1.27	4.2263	17.163	$P\bar{3}m1$	$\text{Ge}_2\text{Sb}_2\text{Te}_5$
Film 4	16.4	28.4	55.4	3.31	0.59	1.05	4.2385	40.932	$R\bar{3}m$	GeSb_2Te_4
Film 5	10.1	35.6	54.3	Not deter mined	0.20	0.70	4.2511	41.435		

Based on the results of X-ray phase analysis (Fig. 2(a)), Films 1, 2, 4, and 5 belong to the hexagonal crystal system with the space group of $R\bar{3}m$, except for Film 3, which belongs to the $P\bar{3}m1$ space group. Phase identification was carried out considering the elemental composition investigated by the EDS detector of the electron microscope. Based on these data, Films 1 and 2 have the composition of $\text{Ge}_3\text{Sb}_2\text{Te}_6$, Film 3 corresponds to the $\text{Ge}_2\text{Sb}_2\text{Te}_5$ phase, and Films 4 and 5 are GeSb_2Te_4 . Therefore, a source-to-substrate distance of 10–13 cm results in the deposition of GST with Ge/Sb ratio < 1 , whereas a distance of 13–14 cm yields GST with a Ge/Sb ratio of 1, and a distance of 14–16 cm leads to the formation of GST with Ge/Sb ratio > 1 . Moreover, X-ray phase analysis also reveals that in Films 2, 3, and 4, the peak corresponding to the (110) crystallographic plane is significantly enhanced compared to standard reference patterns, indicating a preferential grain orientation in these samples. Correlating these XRD results with the observed grain morphology suggests that the anisotropic plate-like crystallites are primarily oriented with their lateral facets exposed. Notably, numerous lateral facets can be associated with the (110) planes identified in the diffraction patterns. In contrast, for Film 5, the (110) peak is not enhanced, as the film underwent recrystallization, which diminished its anisotropy.

The space groups and corresponding lattice parameters are summarized in Table 1. The obtained lattice parameters are consistent with the values calculated in [33], where a dependence between the average interlayer distance and the cation-to-anion ratio for GeTe and Sb_2Te_3 binary compounds was

established. Therefore, the observed variations in lattice parameters can be attributed to differences in the cation-to-anion ratio within the layered crystal structure of the GST compounds.

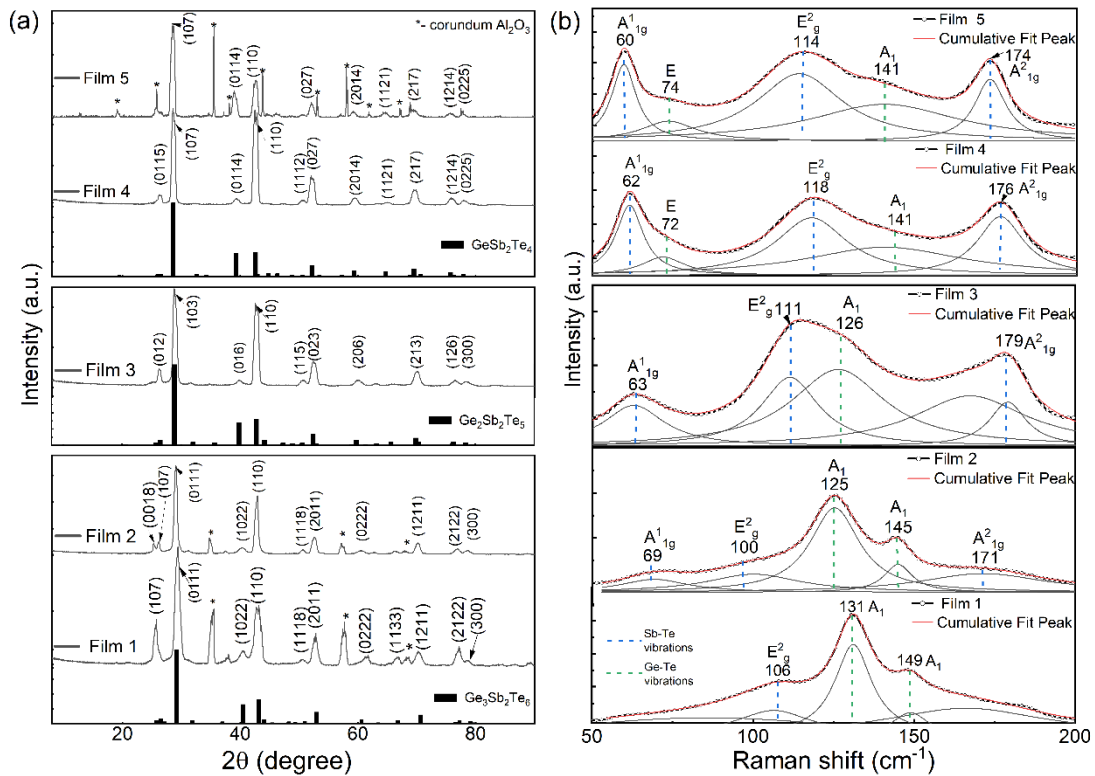


Fig. 2. Characterization spectra of the films obtained via GIXRD analysis (a) and Raman spectroscopy (b). The reference cards for the identified phases, along with the corresponding XRD diffractograms, are provided from the PDF-2 database: Card No. 01-077-6262 for $\text{Ge}_3\text{Sb}_2\text{Te}_6$, Card No. 01-073-7758 for $\text{Ge}_2\text{Sb}_2\text{Te}_5$, and Card No. 01-089-1064 for GeSb_2Te_4 . The Raman spectra were analyzed using Lorentzian function fitting.

The hexagonal phase of GST adopts a layered tetradymite structure inherited from Sb_2Te_3 . The stacking arrangement is influenced by the ratio of GeTe insertions. For $(\text{GeTe})_n(\text{Sb}_2\text{Te}_3)$ ($n \geq 1$), the structure consists of identical Sb_2Te_3 slabs with n -GeTe insertions forming layers stacked along the c -axis via van der Waals gaps. Each slab contains $(2n + 5)$ layers, as each GeTe insertion introduces two additional layers [34]. The $\text{Ge}_3\text{Sb}_2\text{Te}_6$, $\text{Ge}_2\text{Sb}_2\text{Te}_5$, and GeSb_2Te_4 structures identified in the films represent the lowest-energy configurations for the examined Ge/Sb compositions, aligning with previous reports [35].

Although GST films have been extensively studied, a comprehensive Raman characterization of their crystalline phases remains limited. In the current study, we present a Raman analysis of crystalline GST films with varying structural features (Fig. 2(b)). In particular, Raman spectra of the crystalline GST films reveal characteristic vibrational modes associated with both Ge-Te and Sb-Te bonds, enabling the identification of structural differences across the compositional gradient. The $\text{Ge}_3\text{Sb}_2\text{Te}_6$, $\text{Ge}_2\text{Sb}_2\text{Te}_5$, and GeSb_2Te_4 structures corresponding to $\text{Ge/Sb} > 1$, $= 1$, and < 1 , respectively, can be described in terms of n -GeTe units ($n = 3, 2$, and 1) within the $(\text{GeTe})_n(\text{Sb}_2\text{Te}_3)$ framework. The Raman spectrum of $\text{Ge}_3\text{Sb}_2\text{Te}_6$ (Films 1 and 2) is characterized by A_1 modes corresponding to corner-sharing and edge-sharing $\text{GeTe}_{4-n}\text{Ge}_n$ ($n = 0 - 3$) tetrahedra [14, 36], observed at $\sim 131 \text{ cm}^{-1}$ and $\sim 149 \text{ cm}^{-1}$ for Film 1 and at 125 cm^{-1} and 145 cm^{-1} for Film 2. These features reflect the dominance of Ge-Te vibrational modes in $\text{Ge}_3\text{Sb}_2\text{Te}_6$, which contains three GeTe units per Sb_2Te_3 unit. In $\text{Ge}_2\text{Sb}_2\text{Te}_5$ (Film 3), both Ge-Te and Sb-Te vibrational modes are observed. The presence of the A_1 corner-sharing $\text{GeTe}_{4-n}\text{Ge}_n$ ($n = 0 - 3$)

tetrahedra mode at 126 cm^{-1} , along with modes A_{1g}^1 at 63 cm^{-1} , E_g^2 at 111 cm^{-1} , and A_{1g}^2 at 179 cm^{-1} of Sb_mTe_3 ($m = 1, 2$) [14, 36], indicates a balanced contribution from both Ge-Te and Sb-Te subsystems. GeSb_2Te_4 (Films 4 and 5) exhibits dominant Sb-Te vibrational modes. In Film 4, A_{1g}^1 appears at 62 cm^{-1} , E_g^2 at 118 cm^{-1} , and A_{1g}^2 at 176 cm^{-1} ; in Film 5, each of these modes redshifts by approximately 2 cm^{-1} , suggesting a more ordered Sb_2Te_3 -like lattice. Also, Ge-Te vibrational features are presented, with the E and A_1 modes appearing at 72 cm^{-1} and 141 cm^{-1} in Film 4 and at 74 cm^{-1} and 141 cm^{-1} in Film 5. Their reduced intensity further reflects the prevailing Sb_2Te_3 -like structural character. Variations in the Raman modes correlate with the relative GeTe and Sb_2Te_3 content, reflecting structural gradient across the films.

Based on these data, the deposition process led to the gradual formation of GST films. To explain this process, the vapor pressures of the binary compounds GeTe and Sb_2Te_3 , which constitute GST alloys, were analyzed. A review of the literature revealed that at a temperature of 550°C , the vapor pressure of GeTe is three times higher than that of Sb_2Te_3 (8.9 Pa [37] against 2.9 Pa [38]), facilitating the transport of germanium telluride over a greater distance from the source and enriches the more distant substrates with GeTe. Additionally, the temperature gradient, characterized by a decrease in temperature with increasing source-to-substrate distance, likely leads to reduced molecular kinetic energy, thereby contributing to the variation in film thicknesses during the deposition process [39, 40]. Consequently, a small local chemical gradient results in the formation of in-plane heterostructure crystalline films composed of the most stable GST structures, as shown in the compositional diagram (Fig. 3(a)). The obtained crystalline films lie at the pseudobinary line between GeTe and Sb_2Te_3 .

Further, the electrical and optical properties of the above-mentioned films were studied (Fig. 3(b, c)). As is known, the electrical resistivity $\rho = \frac{1}{nq\mu}$ where n is the carrier concentration, q is the carrier charge, and μ is the carrier mobility [41]. Despite a similar carrier concentration at room temperature reported in [3, 42] for $\text{Ge}_3\text{Sb}_2\text{Te}_6$, $\text{Ge}_2\text{Sb}_2\text{Te}_5$, and GeSb_2Te_4 , the synthesized films exhibit notable differences in resistivity, which we believe correlate with crystallite size rather than the composition of the film. $\text{Ge}_3\text{Sb}_2\text{Te}_6$ films with the smallest plates show the highest resistivity ($\sim 17.04 \times 10^{-5}\ \Omega\cdot\text{m}$), while GeSb_2Te_4 films with larger plates exhibit lower values ($\sim 3.50 \times 10^{-5}\ \Omega\cdot\text{m}$). This trend reflects reduced carrier scattering at grain boundaries with increasing plate size, thereby enhancing carrier mobility. So, the observed differences in resistivity among the films are primarily attributed to variations in crystallite size, with larger plates leading to reduced grain boundary scattering and enhanced carrier mobility.

The absorption spectra of proposed crystalline GST compositions were measured at normal incidence of light in the infrared range at $950\text{--}1600\text{ nm}$. Remarkably, the evaluation of the absorbance normalized to a film thickness (A/t) for $\text{Ge}_3\text{Sb}_2\text{Te}_6$, $\text{Ge}_2\text{Sb}_2\text{Te}_5$, and GeSb_2Te_4 films revealed values ranging from ~ 0.5 to $\sim 0.98\ \mu\text{m}^{-1}$. The films exhibit broadband absorption behavior across the NIR region. The $\text{Ge}_2\text{Sb}_2\text{Te}_5$ film had the highest absorption ($0.88 \div 0.98\ \mu\text{m}^{-1}$), whereas $\text{Ge}_3\text{Sb}_2\text{Te}_6$, particularly the sample with smaller crystallites, had the lowest absorption ($0.34 \div 0.25\ \mu\text{m}^{-1}$). The absorption for GeSb_2Te_4 films stayed between $\text{Ge}_3\text{Sb}_2\text{Te}_6$ and $\text{Ge}_2\text{Sb}_2\text{Te}_5$, varying with surface morphology. Film 5, characterized by partially fused plates, exhibits absorption in the range 0.55 to $0.5\ \mu\text{m}^{-1}$, whereas Film 4 demonstrates higher absorption values, ranging from 0.64 to $0.71\ \mu\text{m}^{-1}$. The reflectance of the films normalized to a film thickness was also measured (Fig. S4). These variations are attributed to compositional differences and film morphology: An increase in crystallite size improves light absorption by minimizing scattering at grain boundaries. Among the above-mentioned structures, $\text{Ge}_2\text{Sb}_2\text{Te}_5$ was expected to exhibit high absorbance. Furthermore, additional absorption measurements for the above-mentioned films on the KBr substrate were performed in the $6\text{--}20\ \mu\text{m}$ range, where the films showed strong absorption (Fig. S5).

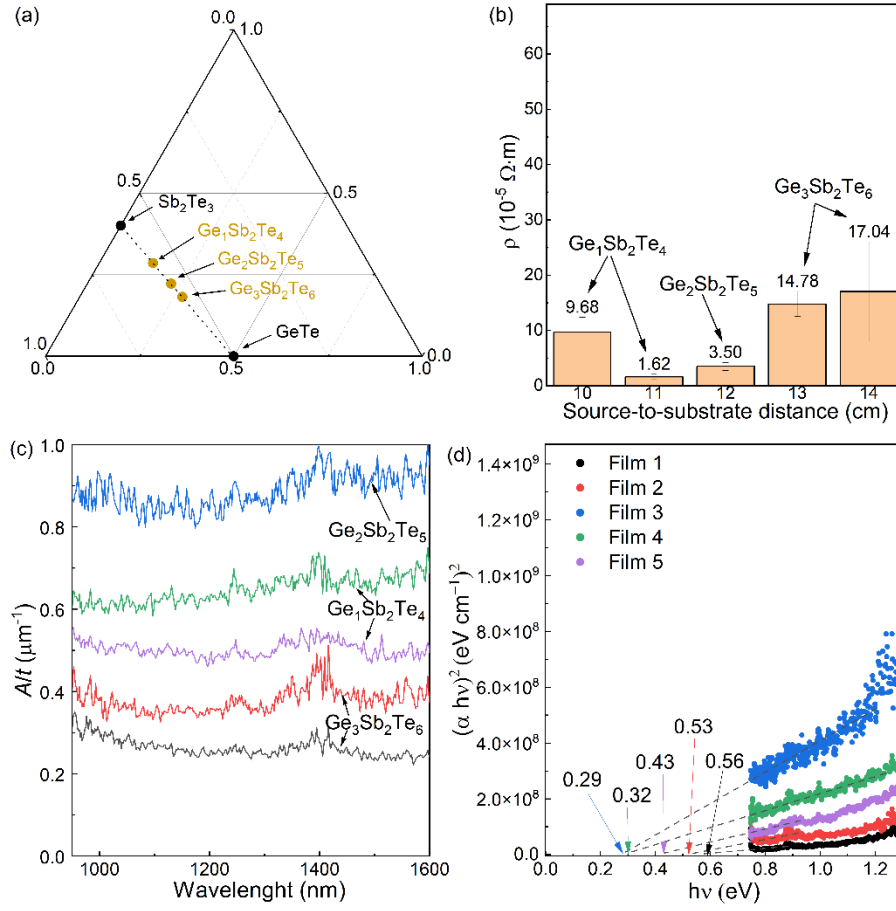


Fig. 3. (a) Compositional diagram of Ge–Sb–Te system indicating the positions of the synthesized films along the Sb₂Te₃–GeTe tie line. (b) The dependence of specific electrical resistivity, including relative errors on the source-to-substrate distance. The sheet resistance was measured 10 times per film. (c) The thickness-normalized absorption spectra measured in the range of 950–1600 nm. All measurements were conducted at room temperature. (d) Estimation of the optical band gap of the synthesized GST films using Tauc plot analysis based on their absorbance spectra.

The optical bandgaps of the crystalline GST films were extracted from absorption spectra using Tauc plot analysis. The studies employed a Tauc exponent of $r = 1/2$ corresponding to direct allowed electronic transitions in crystalline semiconductors [43, 44]. Band structure calculations reveal minor differences between the indirect and direct bandgaps in the crystalline phases of the (GeTe)_n(Sb₂Te₃) system [45]. Fig. 3(d) indicates that the minimum optical band gap of 0.29 eV was obtained for the Ge₂Sb₂Te₅ film. GeSb₂Te₄-based films (Films 4 and 5) exhibited optical band gaps of 0.32 eV and 0.43 eV, respectively. Finally, the Ge₃Sb₂Te₆ films (Films 1 and 2) demonstrated wider band gaps of 0.56 eV and 0.53 eV, respectively. Previous reports revealed that hexagonal Ge₂Sb₂Te₅ and many other compositions within the (GeTe)_n(Sb₂Te₃) system behave as degenerate *p*-type semiconductors with the Fermi level located right above the valence band [46]. So, the optical bandgap is typically smaller, with values of 0.24 to 0.6 eV for the crystalline phase [3, 47, 48]. Although amorphous GST materials usually exhibit a direct bandgap (0.7–0.8 eV) and crystalline GST show indirect bandgaps (0.4–0.6 eV) [32], the strain at the grain boundaries may contribute to the modification of the electronic band structure leading to a shift toward direct bandgap behavior similar to that in [49, 50].

Another key aspect of these materials involves the texture-dependent anisotropic properties. Particularly, it is well established that two-dimensional materials with layered crystal structures exhibit pronounced anisotropic grain growth primarily due to the disparity in bonding within and between the

layers: covalent in-plane and van der Waals out-of-plane, respectively [51]. In the case of our hexagonal GST films, the preferential orientation corresponds to the lateral (110) plane being parallel to the substrate surface. Given the layered nature of the crystal structure, charge carrier transport is expected to proceed more efficiently along the covalently bonded *ab* plane than along the *c*-axis owing to reduced carrier scattering in the in-plane direction. This behavior is in agreement with numerous reports on the anisotropic properties of two-dimensional chalcogenide materials [51-53]. Regarding the effect of texture on optical properties, it has been shown that preferential orientation can significantly impact the reflectance. Specifically, literature [54] reports an increase in optical reflectance associated with a texture transition from the (11 \bar{l}) plane to the (00*c*) plane in Sn-doped crystalline GST films. Thus, in the case of our films, the optical reflectance associated with the (11 \bar{l}) orientation is expected to be reduced compared to that from the *ab* planes.

4. Conclusion

A fast and efficient approach was developed for the CVD synthesis of gradient crystalline GST films with varying Ge/Sb compositions. By simply adjusting the source-to-substrate distance without changing the precursor, the films with compositions of Ge₃Sb₂Te₆, Ge₂Sb₂Te₅, and GeSb₂Te₄ were simultaneously deposited onto substrates potentially allowing controllable formation of planar GST gradient heterostructures. The films' structural properties, electrical resistivity, and optical absorbance were analyzed to evaluate their potential applications in electronic and optoelectronic devices. In particular, an in-depth analysis of the composition, microstructure, and morphology of the GST films uncovered variations in elemental distribution, morphology, and grain sizes relative to their distance from the source crystal adjusted during growth. We believe that using a large-area substrate during the growth of GST films may allow for the potential fabrication of gradient IR filters—exhibiting high central absorption and lower absorption at the edges—which may be beneficial for photonic devices, such as optical modulators, beam shaping elements, and photonic circuits with built-in spatial control functionalities or sensors requiring spatially resolved control of signal intensity.

References

- [1] W. H. Pernice, H. Bhaskaran, Photonic nonvolatile memories using phase change materials, Appl. Phys. Lett. 101 (2012) 171101. <https://doi.org/10.1063/1.4758996>.
- [2] P. Prabhathan, K. V. Sreekanth, J. Teng, J. H. Ko, Y. J. Yoo, H. H. Jeong, Y. Lee, S. Zhang, T. Cao, C.-C. Popescu, B. Mills, T. Gu, Z. Fang, R. Chen, H. Tong, Y. Wang, Q. He, Y. Lu, Z. Liu, H. Yu, A. Mandal, Y. Cui, A. S. Ansari, V. Bhingardive, M. Kang, C. K. Lai, M. Merklein, M. J. Müller, Y. M. Song, Z. Tian, J. Hu, M. Losurdo, A. Majumdar, X. Miao, X. Chen, B. Gholipour, K. A. Richardson, B. J. Eggleton, M. Wuttig, R. Singh, (2023). Roadmap for phase change materials in photonics and beyond, Isci. 26(10) (2023) 107946. <https://doi.org/10.1016/j.isci.2023.107946>.
- [3] Y. Jiang, T. R. Wei, X. Shi, Beyond phase-change materials: Pseudobinary (GeTe)_n(Sb₂Te₃)_m alloys as promising thermoelectric materials, Mater. Today Phys. 36 (2023) 101167. doi.org/10.1016/j.mtphys.2023.101167.
- [4] A. Zareizadeh, N. Nozhat, GST plasmonic gap structure investigation as a switch and sensor, Appl. Opt. 62(23) (2023) 6156-6162. <https://doi.org/10.1364/AO.497742>.
- [5] L. Wang, S. R. Lu, J. Wen, Recent advances on neuromorphic systems using phase-change materials. Nanoscale Res. Lett. 12 (2017) 1-22. <https://doi.org/10.1186/s11671-017-2114-9>.
- [6] M. T. Emrose, E. L. Payne, C. You, G. Veronis, Broadband switchable infrared absorbers using phase-change materials, Opt. Mater. Express. 14(3) (2024) 577-591. <https://doi.org/10.1364/OME.509650>.
- [7] G. Bulai, O. Pompilian, S. Gurlui, P. Nemec, V. Nazabal, N. Cimpoesu, B. Chazallon, C. Focsa, Ge-Sb-Te chalcogenide thin films deposited by nanosecond, picosecond, and femtosecond laser ablation, Nanomater. 9(5) (2019) 676. <https://doi.org/10.3390/nano9050676>.

- [8] I. D., Simandan, F. Sava, A. T. Buruiana, A. C. Galca, N. Becherescu, I. Burducea, C. Mihai, A. Velea, Influence of deposition method on the structural and optical properties of $\text{Ge}_2\text{Sb}_2\text{Te}_5$, *Mater.* 14(13) (2021) 3663. <https://doi.org/10.3390/ma14133663>.
- [9] H. Hardtdegen, M. Mikulics, S. Rieß, M. Schuck, T. Saltzmann, U. Simon, M. Longo, Modern chemical synthesis methods towards low-dimensional phase change structures in the Ge–Sb–Te material system, *Prog. Cryst. Growth Charact. Mater.* 61 (2015) 27–45. <https://doi.org/10.1016/j.pcrysgrow.2015.10.001>.
- [10] J. H. Jeong, J. H. Park, Y. M. Lee, U. Hwang, H. K. Kim, D. S. Kil, D. J. Choi, Study of Ge–Sb–Te and Ge–Te cocktail sources to improve an efficiency of multi-line CVD for phase change memory, *Mater. Sci. Semicond. Process.* 40 (2015) 50–57. <https://doi.org/10.1016/j.mssp.2015.06.027>.
- [11] L. B. Freund, S. Suresh, *Thin film materials: stress, defect formation and surface evolution*, Cambridge University Press, New York, 2004.
- [12] T. Zhang, L. Fu, Controllable chemical vapor deposition growth of two-dimensional heterostructures, *Chem*, 4(4) (2018) 671–689. <https://doi.org/10.1016/j.chempr.2017.12.006>.
- [13] M. Alahmadi, F. Mahvash, T. Szkopek, M. Sij, A two-step chemical vapor deposition process for the growth of continuous vertical heterostructure $\text{WSe}_2/\text{h-BN}$ and its optical properties, *RSC Adv.* 11 (2021) 16962–16969. <https://doi.org/10.1039/D1RA02523F>.
- [14] J. Du, Z. Mu, L. Li, J. Li, A Raman study on nanosecond-laser-induced multilevel switching of $\text{Ge}_2\text{Sb}_2\text{Te}_5$ thin films. *Opt. Laser Technol.* 144 (2021) 107393. <https://doi.org/10.1016/j.optlastec.2021.107393>.
- [15] H. Zhang, X. Yang, L. Lu, J. Chen, B. M. A. Rahman, L. Zhou, Comparison of the phase change process in a GST-loaded silicon waveguide and MMI. *Opt. Express* 29(3) (2021) 3503–3514. <https://doi.org/10.1364/OE.413660>.
- [16] R.-J. Zhu, R.-Z. Zhao, K. Gao, Z.-R. Zhang, Q. He, H. Tong, X.-S. Miao, High-Stability van Der Waals Structures of $\text{GeTe}/\text{Sb}_2\text{Te}_3$ Superlattices for 100× Increased Durability Phase-Change Memory (PCM) by Low-Temperature Atomic Layer Deposition, *Adv. Funct. Mater.* 34 (2024) 2408897. <https://doi.org/10.1002/adfm.202408897>.
- [17] J.-J. Wang, H.-M. Zhang, X.-D. Wang, L. Lu, C. Jia, W. Zhang, R. Mazzarello, In-Plane Twinning Defects in Hexagonal GeSb_2Te_4 , *Adv. Mater. Technol.* 7 (2022) 2200214. <https://doi.org/10.1002/admt.202200214>.
- [18] R.-J. Zhu, R.-Z. Zhao, K. Gao, H. Tong, X.-S. Miao, Low-Temperature Atomic Layer Deposition of $\text{GeTe}/\text{Sb}_2\text{Te}_3$ Superlattice with High-Quality van der Waals Structure, *Phys. Status Solidi RRL* 18 (2024) 2400371. <https://doi.org/10.1002/pssr.202400371>.
- [19] D. Térébénec, F. Hippert, N. Bernier, N. Castellani, P. Noé, $\text{GeTe}/\text{Sb}_2\text{Te}_3$ Super-Lattices: Impact of Atomic Structure on the RESET Current of Phase-Change Memory Devices, *Adv. Electron. Mater.* 11 (2024) 2400290. <https://doi.org/10.1002/aelm.202400290>.
- [20] Y. Gan, N. Miao, J. Zhou, Z. Sun, New two-dimensional Ge–Sb–Te semiconductors with high photovoltaic performance for solar energy conversion, *J. Mater. Chem. C* 10(44) (2022) 16813–16821. <https://doi.org/10.1039/D2TC04085A>.
- [21] S. G. Sarwat, N. Youngblood, Y. Y. Au, J. A. Mol, C. D. Wright, H. Bhaskaran, Engineering interface-dependent photoconductivity in $\text{Ge}_2\text{Sb}_2\text{Te}_5$ nanoscale devices, *ACS Appl. Mater. Interfaces* 10(51) (2018) 44906–44914. <https://doi.org/10.1021/acsami.8b17602>.
- [22] X. Zhao, X. Shang, S. Li, L. Wang, Y. He, H. Tan, Y. Wei, S. Fu, G. Wang, W. Zhang, C. Bai, N. Xu, C. Lu, H. Zhang, Q-switched operation of erbium-doped fiber laser based on $\text{Ge}_2\text{Sb}_2\text{Te}_5$ saturable absorber under positive and negative net dispersion conditions, *Opt. Mater.* 163 (2025) 116946. <https://doi.org/10.1016/j.optmat.2025.116946>.
- [23] Z. Guo, X. Yang, F. Shen, Q. Zhou, J. Gao, K. Guo, Active-tuning and polarization-independent absorber and sensor in the infrared region based on the phase change material of $\text{Ge}_2\text{Sb}_2\text{Te}_5$ (GST), *Sci. Rep.* 8(1) (2018) 12433. <https://doi.org/10.1038/s41598-018-30550-2>.
- [24] S. K. Verma, M. Jangra, A. Datta, S. K. Srivastava, Experimental demonstration of $\text{Ge}_2\text{Sb}_2\text{Te}_5$ loaded 1-D plasmonic metasurface perfect absorber for near-IR wavelength regime, *Opt. Lett.* 49(16) (2024) 4638–4641. <https://doi.org/10.1364/OL.532638>.
- [25] J. Parra, J. Navarro-Arenas, M. Kovylyna, P. Sanchis, Impact of GST thickness on GST-loaded silicon waveguides for optimal optical switching, *Sci. Rep.* 12 (2022) 9774. <https://doi.org/10.1038/s41598-022-13848-0>.

- [26] M. Wuttig, H. Bhaskaran, T. Taubner, Phase-change materials for non-volatile photonic applications, *Nat. Photonics* 11 (2017) 465–476. <https://doi.org/10.1038/nphoton.2017.126>.
- [27] S. Hu, C. Wang, S. Du, Z. Han, N. Hu, C. Gu, Laser-induced reconfigurable wavefront control with a structured $\text{Ge}_2\text{Sb}_2\text{Te}_5$ -based metasurface, *Commun. Phys.* 7 (2024) 346. <https://doi.org/10.1038/s42005-024-01846-9>.
- [28] A. B. Talochkin, K. A. Kokh, O. E. Tereshchenko, Optical phonons of GeSbTe alloys: Influence of structural disorder, *J. Alloys Compd.* 942 (2023) 169122. <https://doi.org/10.1016/j.jallcom.2023.169122>.
- [29] Y. Yao, X. Zhan, C. Ding, F. Wang, Y. Wang, J. Yang, Z. Wang, J. He, One-step method to simultaneously synthesize separable Te and GeTe nanosheets. *Nano Res.* 15(7) (2022) 6736–6742. <https://doi.org/10.1007/s12274-022-4330-6>.
- [30] G. Wang, Q. Nie, X. Shen, R. P. Wang, Li. Wu, J. Fu, T. Xu, S. Dai, Phase change behaviors of Zn-doped $\text{Ge}_2\text{Sb}_2\text{Te}_5$ films, *Appl. Phys. Lett.* 101 (2012) 051906. <http://dx.doi.org/10.1063/1.4742144>.
- [31] R. I. Romanov, I. V. Zabrosae, A. A. Chouprik, D. I. Yakubovsky, M. K. Tatmyshevskiy, V. S. Volkov, A. M. Markeev, Temperature-dependent structural and electrical properties of metal-organic CVD MoS_2 films, *Nanomaterials* 13(19) (2023) 2712. <https://doi.org/10.3390/nano13192712>.
- [32] J. H. Jeong, J. H. Park, Y. M. Lee, U. Hwang, H. K. Kim, D. S. Kil, D. J. Choi, Study of Ge–Sb–Te and Ge–Te cocktail sources to improve an efficiency of multi-line CVD for phase change memory. *Mater. Sci. Semicond. Process.* 40 (2015).50–57. <https://doi.org/10.1016/j.mssp.2015.06.027>.
- [33] O. G. Karpinsky, L. E. Shelimova, M. A. Kretova, J. P. Fleurial, An X-ray study of the mixed-layered compounds of $(\text{GeTe})_n(\text{Sb}_2\text{Te}_3)_m$ homologous series, *J. Alloys Compd.* 268(1-2) (1998) 112–117. [https://doi.org/10.1016/S0925-8388\(97\)00625-7](https://doi.org/10.1016/S0925-8388(97)00625-7).
- [34] T. Rosenthal, M. N. Schneider, C. Stiewe, M. Döblinger, O. Oeckler, Real structure and thermoelectric properties of GeTe-rich germanium antimony tellurides, *Chem. Mater.* 23(19) (2011) 4349–4356. <https://doi.org/10.1021/cm201717z>.
- [35] J. L. Da Silva, A. Walsh, H. Lee, Insights into the structure of the stable and metastable $(\text{GeTe})_m(\text{Sb}_2\text{Te}_3)_n$ compounds, *Phys. Rev. B: Condens. Matter Mater. Phys.* 78(22) (2008) 224111. <http://doi.org/10.1103/PhysRevB.78.224111>.
- [36] A. A. Burtsev, N. N. Eliseev, V. A. Mikhalevsky, A. V. Kiselev, V. V. Ionin, V. V. Grebenev, D.N. Karimov, A. A. Lotin, Physical properties’ temperature dynamics of GeTe, $\text{Ge}_2\text{Sb}_2\text{Te}_5$ and $\text{Ge}_2\text{Sb}_2\text{Se}_4\text{Te}_1$ phase change materials, *Mater. Sci. Semicond. Process.* 150 (2022) 106907. <https://doi.org/10.1016/j.mssp.2022.106907>.
- [37] C. Hirayama, The vapor pressure of germanium telluride, *J. Phys. Chem.* 66(8) (1962) 1563–1565. <https://doi.org/10.1021/j100814a519>.
- [38] V. Piacente, P. Scardala, D. Ferro, Study of the vaporization behaviour of Sb_2S_3 and Sb_2Te_3 from their vapour pressure measurements, *J. Alloys Compd.* 178 (1992) 101–115. [https://doi.org/10.1016/0925-8388\(92\)90251-4](https://doi.org/10.1016/0925-8388(92)90251-4).
- [39] L. Huang, J. Dong, Y. Hu, J. Yang, X. Peng, H. Wang, C. Zhu, R. Tang, Y. Zhang, T. Chen, Temperature-Gradient Solution Deposition Amends Unfavorable Band Structure of $\text{Sb}_2(\text{S}, \text{Se})_3$ Film for Highly Efficient Solar Cells, *Angew. Chem.* 136(36) (2024) e202406512. <https://doi.org/10.1002/anie.202406512>.
- [40] K. Aryana, C. C. Popescu, H. Sun, K. Aryana, H. J. Kim, M. Julian, M. R. Islam, C. A. Ríos Ocampo, T. Gu, J. Hu, P. E. Hopkins, Thermal Transport in Chalcogenide-Based Phase Change Materials: A Journey from Fundamental Physics to Device Engineering, *Adv. Mater.* 37(11) (2025) 2414031. <https://doi.org/10.1002/adma.202414031>.
- [41] W.D. Callister Jr., D.G. Rethwisch, *Materials Science and Engineering*, tenth ed., John Wiley & Sons, 2020.
- [42] T. R. Wei, P. Hu, H. Chen, K. Zhao, P. Qiu, X. Shi, L. Chen, Quasi-two-dimensional GeSbTe compounds as promising thermoelectric materials with anisotropic transport properties, *Appl. Phys. Lett.* 114(5) (2019) 053903. <https://doi.org/10.1063/1.5083863>.
- [43] B. S. Lee, J. R. Abelson, S. G. Bishop, D. H. Kang, B. K. Cheong, K. B. Kim, Investigation of the optical and electronic properties of $\text{Ge}_2\text{Sb}_2\text{Te}_5$ phase change material in its amorphous, cubic, and hexagonal phases, *J. Appl. Phys.* 97(9) (2005) 093509. <https://doi.org/10.1063/1.1884248>.
- [44] H. B. Yao, L. P. Shi, T. C. Chong, P. K. Tan, X. S. Miao, Optical transition of chalcogenide phase-change thin films, *Jpn. J. Appl. Phys.* 42(2S) (2003) 828 <https://doi.org/10.1143/JJAP.42.828>.

- [45] J. W. Park, S. H. Eom, H. Lee, J. L. Da Silva, Y. S. Kang, T. Y. Lee, Y. H. Khang, Optical properties of pseudobinary GeTe, $\text{Ge}_2\text{Sb}_2\text{Te}_5$, GeSb_2Te_4 , GeSb_4Te_7 , and Sb_2Te_3 from ellipsometry and density functional theory, *Phys. Rev. B: Condens. Matter Mater. Phys.* 80(11) (2009) 115209. <http://doi.org/10.1103/physrevb.80.115209>.
- [46] Z. Sun, S. Kyrsta, D. Music, R. Ahuja, J. M. Schneider, Structure of the Ge–Sb–Te phase-change materials studied by theory and experiment, *Solid State Commun.* 143(4-5) (2007) 240-244. <https://doi.org/10.1016/j.ssc.2007.05.018>.
- [47] J. Kellner, G. Bihlmayer, M. Liebmann, S. Otto, C. Pauly, J. E. Boschker, M. Morgenstern, Mapping the band structure of GeSbTe phase change alloys around the Fermi level, *Commun. Phys.* 1 (2018) 5. <https://doi.org/10.1038/s42005-018-0005-8>.
- [48] V. E. Madhavan, M. Carignano, A. Kachmar, K. S. Sangunni, Crystallization properties of arsenic doped GST alloys, *Sci. Rep.* 9(1) (2019) 12985. <https://dx.doi.org/10.1038/s41598-019-49168-z>.
- [49] J. Miao, P. Wang, P. Zhou, S. Huang, D. Qian, Y. Yuan, R. Lan, Remarkable anisotropy in rhombohedral $\text{Ge}_2\text{Sb}_2\text{Te}_5$ compound: A promising thermoelectric material with multiple conduction bands and acoustic-optical branches coupling, *J. Alloys Compd.* 900 (2022) 163471. <https://doi.org/10.1016/j.jallcom.2021.163471>.
- [50] P. Zhou, R. Lan, P. Wang, J. Miao, S. Huang, Y. Yuan, J. Xu, Tuned electronic band structure and intensified phonon scattering of $\text{Ge}_2\text{Sb}_2\text{Te}_5$ by strain engineering for thermoelectric performance, *Mater. Today Commun.* 35 (2023) 105839. <https://doi.org/10.1016/j.mtcomm.2023.105839>.
- [51] S. Zhao, B. Dong, H. Wang, H. Wang, Y. Zhang, Z. Vitto Han, H. Zhang, In-plane anisotropic electronics based on low-symmetry 2D materials: progress and prospects, *Nanoscale Adv.* 2 (2020) 109-139. <https://doi.org/10.1039/C9NA00623K>.
- [52] A. Vasil'ev, M. Yaprincev, O. Ivanov, E. Danshina, Anisotropic thermoelectric properties of $\text{Bi}_{1.9}\text{Lu}_{0.1}\text{Te}_{2.7}\text{Se}_{0.3}$ textured via spark plasma sintering, *Solid State Sci.* 84 (2018) 28-43. <https://doi.org/10.1016/j.solidstatesciences.2018.08.004>.
- [53] S. Chen, K. Liu, T. Luo, L. Liao, Z. Yang, S. Zhong, J. Wu, X. Su, P. F. P. Poudeu, Q. Zhang, X. Tang, Structural evolution and thermoelectric performance in $(\text{GeTe})_m(\text{Sb}_2\text{Te}_3)_n$ compounds, *Mater. Today Phys.* 45 (2024) 101455. <https://doi.org/10.1016/j.mtphys.2024.101455>.
- [54] Q. Yin, L. Chen Enhanced optical properties of Sn-doped $\text{Ge}_2\text{Sb}_2\text{Te}_5$ thin film with structural evolution, *J. Alloys Compd.* 770 (2019) 692-700. <https://doi.org/10.1016/j.jallcom.2018.08.169>.

Supplementary Information for
Chemical vapor deposition synthesis of (GeTe)_n(Sb₂Te₃) gradient crystalline films as promising
planar heterostructures

M. Zhezhu^{1,*}, A. Vasil'ev¹, M. Yapyrntsev², E. Ghalumyan³, D. A. Ghazaryan^{4,5}, H. Gharagulyan^{1,3,*}

¹*A.B. Nalbandyan Institute of Chemical Physics NAS RA, Yerevan 0014, Armenia*

²*Belgorod State University, Belgorod 308000, Russia*

³*Institute of Physics, Yerevan State University, Yerevan 0025, Armenia*

⁴*Moscow Center for Advanced Studies, Kulakova str. 20, Moscow 123592, Russia*

⁵*Laboratory of Advanced Functional Materials, Yerevan State University, Yerevan 0025, Armenia*

*The correspondence should be addressed to:

marina.zhezhu@ichph.sci.am and herminegharagulyan@ysu.am

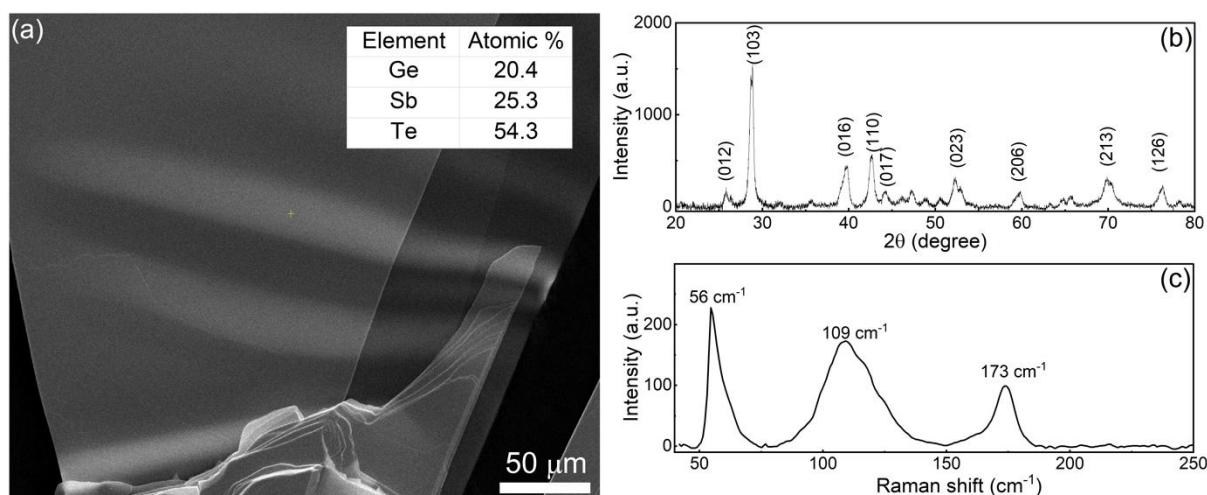


Fig. S1. Characterization of the synthesized target includes SEM analysis of the fracture surface with (a) EDS, (b) XRD analysis, and (c) Raman spectroscopy.

Details of morphological analysis

SEM images revealed variations in grain structure, while AFM measurements provided insights into surface roughness and topographical features. To obtain a statistically reliable l/d ratio, the length and thickness of over 150 individual plates were measured from SEM images. The resulting distributions for both parameters are well described by a unimodal lognormal function, and the corresponding values are presented in Table S1. Additionally, R_{ms} values were determined from $10\ \mu\text{m} \times 10\ \mu\text{m}$ AFM scans.

Table S1. Plate sizes represented by d and l/d ratio of Films 1–4.

Film number	d , nm	l/d
1	143	2.6
2	224	5.2
3	277	7.6
4	543	6.1

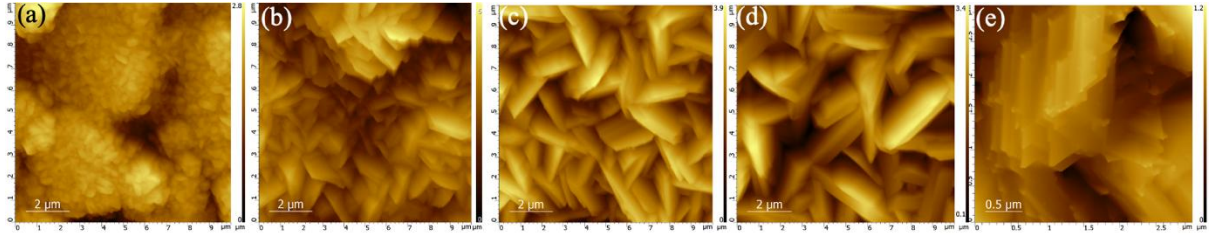


Fig. S2. The AFM images of the film surfaces deposited on each substrate: (a) Film 1, (b) Film 2, (c) Film 3, (d) Film 4, and (e) Film 5.

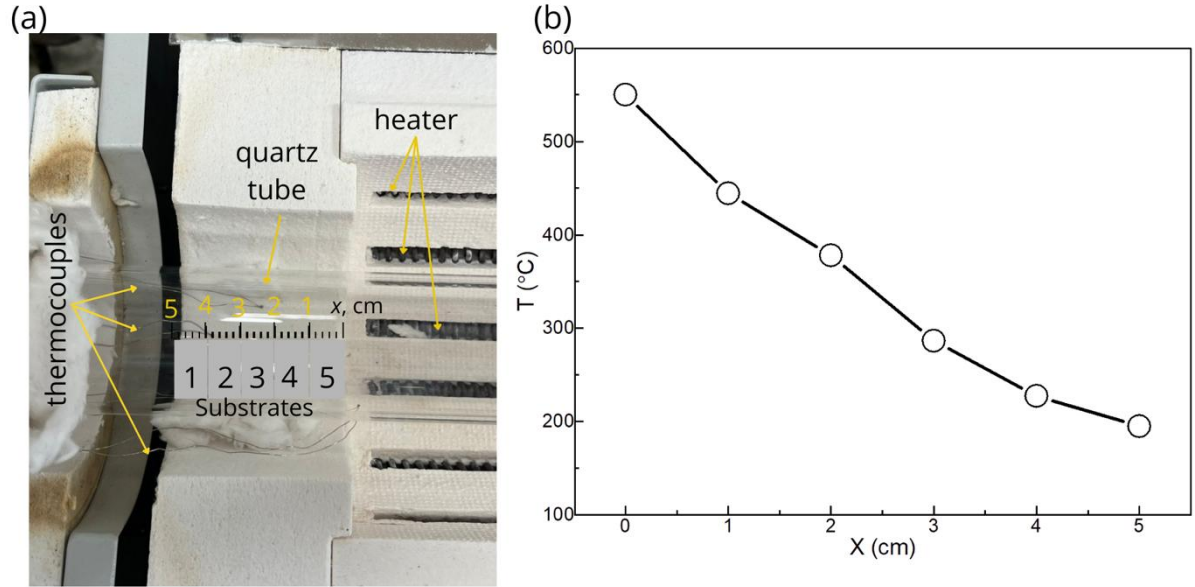


Fig. S3. Control experiment schematic for measuring temperature distribution in the cold zone. (b) Temperature gradient across the cold zone as a function of distance from the hot zone. The segment from 0 to 1 cm corresponds to the position of Film 5; 1–2 cm to Film 4; 2–3 cm to Film 3; 3–4 cm to Film 2; and 4–5 cm to Film 1.

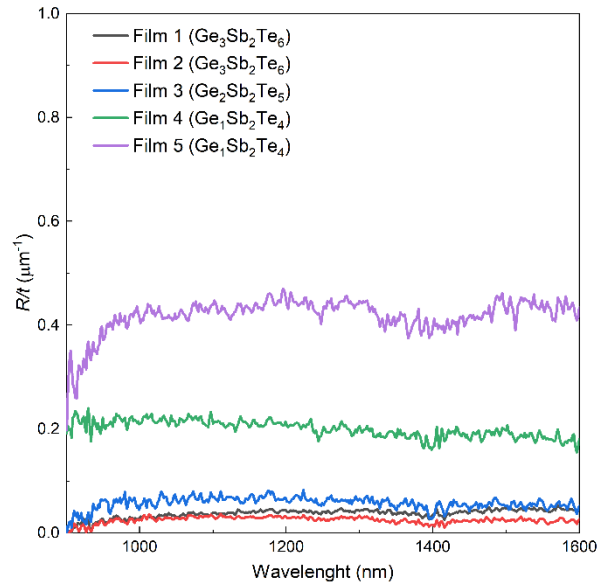


Fig. S4. The thickness-normalized reflectance spectra measured in the range of 950–1600 nm at room temperature.

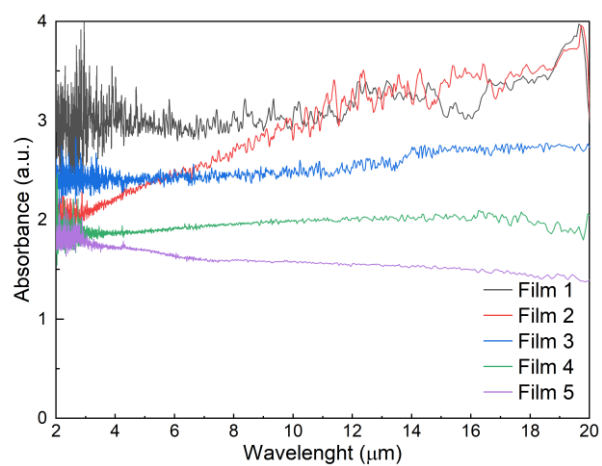


Fig. S5. Absorbance spectra measured on a KBr substrate in the 2–20 μm wavelength range at room temperature.